
CRYSPORMER: PROTEIN STRUCTURE PREDICTION VIA 3D PATTERSON MAPS AND PARTIAL STRUCTURE ATTENTION

Chen Dun*
Rice University
cd46@rice.edu

Qiutai Pan*
Rice University
qp3@rice.edu

Shikai Jin
Rice University
sj52@rice.edu

Ria Stevens
Rice University
Ria.Stevens@rice.edu

Mitchell D. Miller
Rice University
mitchm@rice.edu

George N. Phillips, Jr.
Rice University
georgep@rice.edu

Anastasios Kyrillidis
Rice University
anastasios@rice.edu

ABSTRACT

Determining the structure of a protein has been a decades-long open question. A protein’s three-dimensional structure often poses nontrivial computation costs, when classical simulation algorithms are utilized. Advances in the transformer neural network architecture –such as AlphaFold2– achieve significant improvements for this problem, by learning from a large dataset of sequence information and corresponding protein structures. Yet, such methods only focus on sequence information; other available prior knowledge, such as protein crystallography and partial structure of amino acids, could be potentially utilized. To the best of our knowledge, we propose the first transformer-based model that directly utilizes protein crystallography and partial structure information to predict the electron density maps of proteins. Via two new datasets of peptide fragments (2-residue and 15-residue), we demonstrate our method, dubbed *CrysFormer*, can achieve accurate predictions, based on a much smaller dataset size and with reduced computation costs.

1 INTRODUCTION

Proteins, the biological molecular machines, play a central role in the majority of cellular processes (Tanford & Reynolds, 2004). The investigation of a protein’s structure is a classic challenge in biology, given that its function is dictated by its specific conformation. Proteins comprise long chains of linked, relatively small organic molecules called *amino acids*, with a set of twenty of them considered as standard. However, these underlying polypeptide chains fold into complex three-dimensional structures, as well as into larger assemblies thereof. Consequently, biologists aim to establish a standardized approach for experimentally determining and visualizing the overall structure of a protein at a low cost.

In the past decades, there have been three general approaches to the protein structure problem: *i*) ones that rely on physical experimental measurements, such as X-ray crystallography, NMR, or cryo-electron microscopy; see (Drenth, 2007) for more details; *ii*) protein folding simulation tools based on thermodynamic or kinetic simulation of protein physics (Brini et al., 2020; Sippl, 1990); and, *iii*) evolutionary programs based on bioinformatics analysis of the evolutionary history of proteins (Šali & Blundell, 1993; Roy et al., 2010).

Recent advances in machine learning (ML) algorithms have inspired a fourth direction which is to train a deep neural network model on a combination of a large-scale protein structure data set (i.e.,

*Authors contributed equally.

the Protein Data Bank (wwPDB consortium, 2019)) and knowledge of the amino acid sequences of a vast number of homologous proteins, to directly predict the protein structure from the protein’s amino acid sequence. Recent research projects –such as Alphafold2 (Jumper et al., 2021)– further show that, with co-evolutionary bioinformatic information (e.g., multiple sequence alignments), deep learning can achieve highly accurate predictions in most cases.

Our hypothesis and contributions. While it is true that computational methods of predicting structures without experimentally confirming data are improving, they are not yet complete –in terms of the types of structures that can be predicted– and suffer from lack of accuracy in many of the details (Terwilliger et al., 2023). X-ray crystallographic data continues to be a gold standard for critical details describing chemical interactions of proteins.

Having a robust and accurate way of going directly from an X-ray diffraction pattern to a solved structure would be a strong contribution to the field of X-ray crystallography. Such approaches are missing from the literature, with the exception of Pan et al. (2023), a recent effort on the same problem based on residual convolutional autoencoders.

Here, we present the first transformer-based model that utilizes protein crystallography and partial structure information to directly predict the electron density maps of proteins, going one step beyond such recent approaches. While not yet ready to solve real problems, we demonstrate success on a simplified problem. As a highlight, using a new dataset of small peptide fragments of variable unit cell sizes –a byproduct of this work– we demonstrate that our method, named `CrysFormer`, can achieve more accurate predictions than state of the art (Pan et al., 2023) with less computations.

Some of our findings and contributions are:

- `CrysFormer` is able to process the global information in Patterson maps to infer electron density maps; to the best of our knowledge, along with Pan et al. (2023), these are the first works to attempt this setting.
- `CrysFormer` can incorporate “partial structure” information, when available; we also show that such information could be incorporated in existing solutions that neglected this feature, like the convolutional `U-Net`-based architectures in Pan et al. (2023). However, the `CrysFormer` architecture still leads to better reconstructions.
- In practice, `CrysFormer` achieves a significant improvement in prediction accuracy in terms of both Pearson coefficient and mean phase error, while requiring both a smaller number of epochs to converge and less time taken per epoch.
- This work introduces a new dataset of variable-cell dipeptide fragments, where all of the input Patterson and output electron density maps were derived from the Protein Databank (PDB) (wwPDB consortium, 2019), solved by X-ray Crystallography. We will make this dataset publicly available.

2 PROBLEM SETUP AND RELATED WORK

X-ray crystallography and the crystallographic phase problem. X-ray crystallography has been the most commonly used method to determine a protein’s electron density map¹ for over 100 years (Lattman & Loll, 2008). However, there is an open question, called the crystallographic phase problem, that prevents researchers from utilizing it to predict true structures/electron density maps.

In review, each spot (known as a reflection) in an X-ray crystallography diffraction pattern is denoted by three indices h, k, l , known as Miller indices (Ashcroft & Mermin, 2022). These correspond to sets of parallel planes within the protein crystal’s unit cell that contribute to producing the reflections. The set of possible h, k, l values is determined by the radial extent of the observed diffraction pattern. Any reflection has an underlying mathematical representation, known as a structure factor, dependent on the locations and scattering factors of all the atoms within the crystal’s unit cell. In math:

$$F(h, k, l) = \sum_{j=1}^n f_j \cdot e^{2\pi i(hx_j + ky_j + lz_j)}, \quad (1)$$

where the scattering factor and location of atom j are f_j and (x_j, y_j, z_j) , respectively.

A structure factor $F(h, k, l)$ has both an amplitude and a phase component (denoted by ϕ) and thus can be considered a complex number. Furthermore, suppose we knew both components of the

¹The electron density is a measure of the probability of an electron being present just around a particular point in space; a complete electron density map can be used to obtain a molecular model of the unit cell.

structure factors corresponding to all of the reflections within a crystal’s diffraction pattern. Then, in order to produce an accurate estimate of the electron density at any point (x, y, z) within the crystal’s unit cell, we would only need to take a Fourier transform of all of these structures, as in:

$$\rho(x, y, z) = \frac{1}{V} \cdot \sum_{h,k,l} |F(h, k, l)| \cdot e^{-2\pi i(hx+ky+lz-\phi(h,k,l))}, \quad (2)$$

where V is the volume of the unit cell. The amplitude $|F(h, k, l)|$ of any structure factor is easy to determine, as it is simply proportional to the square root of the measured intensity of the corresponding reflection. However, it is impossible to directly determine the phase $\phi(h, k, l)$ of a structure factor, and this is what is well-known as the crystallographic phase problem (Lattman & Loll, 2008).

Solving the phase problem. Various methods have been developed to solve the crystallography phase problem. The three commonly used methods are isomorphous replacement, anomalous scattering, and molecular replacement (Lattman & Loll, 2008; Jin et al., 2020). Also, what is known as direct methods have been successful for small molecules that diffract to atomic resolution, but they rarely work for protein crystallography, due to the difficulty of resolving atoms as separate objects. Alternative methods have been developed to solve the phase problem based on intensity measurements alone, known as phase retrieval (Guo et al., 2021; Kappeler et al., 2017; Rivenson et al., 2018). However, these methods have not been widely used in X-ray crystallography, because they assume different sampling conditions or were designed for non-crystallographic fields of physics. The iterative non-convex Gerchberg–Saxton algorithm (Fienup, 1982; Zalevsky et al., 1996) is a well-known example of such methods, but requires more measurements than is available in crystallography.

Although adaptations of the Gerchberg–Saxton algorithm have been proposed for crystallography-like settings, they have not been used to solve the phase problem except in special cases where crystals have very high solvent content (He & Su, 2015; He et al., 2016; Kingston & Millane, 2022). More recently, Candes et al. (2013) introduced the `PhaseLift` method, a convex, complex semidefinite programming approach, and Candes et al. (2015) the Wirtinger flow algorithm (Candes et al., 2015), a non-convex phase retrieval method; both these methods have not been applied practically, due to their computationally intensive nature.

3 CRYSTFORMER: USING 3D MAPS AND PARTIAL STRUCTURE ATTENTION

Inspired by (Hurwitz, 2020), we rely on deep learning solutions to directly predict the electron density map of a protein. Later in the text, we demonstrate that such a data-centric method achieves both better accuracy and reduced computational cost.

The Patterson function. We utilize the *Patterson function* (Patterson, 1934), a simplified variation of the Fourier transform from structure factors to electron density, in which all structure factor amplitudes are squared, and all phases are set to zero (i.e., ignored), as in:

$$p(u, v, w) = \frac{1}{V} \cdot \sum_{h,k,l} |F(h, k, l)|^2 \cdot e^{-2\pi i(hu+kv+lw)}. \quad (3)$$

It is important to note the Patterson map can be directly obtained from raw diffraction data without the need for additional experiments, or any other information.

Due to the discrete size of the input and output layers in deep learning models, we can discretize and reformulate the electron density map –and its corresponding Patterson map– as follows: Suppose the electron density map of a molecule in interest is discretized into a $N_1 \times N_2 \times N_3$ 3d grid. The electron density map can then be denoted as $\mathbf{e} \in \mathbb{R}^{N_1 \times N_2 \times N_3}$. The Patterson map is then formulated as follows, where \odot means matrix element-wise multiplication:

$$\mathbf{p} = \Re(\mathcal{F}^{-1}(\mathcal{F}(\mathbf{e}) \odot \mathcal{F}(\hat{\mathbf{e}}))) \approx \Re(\mathcal{F}^{-1}(|\mathcal{F}(\mathbf{e})|^2)).$$

Breaking down the above expression, $\mathcal{F}(\mathbf{e}) \odot \mathcal{F}(\hat{\mathbf{e}}) \approx |\mathcal{F}(\mathbf{e})|^2$ denotes only the magnitude part of the complex signals, as measured through the Fourier transform of the input signal \mathbf{e} . Here, $\hat{\mathbf{e}}$ denotes an inverse-shifted version of \mathbf{e} , where its entries follow the shifted rule as in $\hat{e}_{i,j,k} = e_{N-i, N-j, N-k}$.

Using deep learning. We follow a data-centric approach and train a deep learning model, abstractly represented by $g(\boldsymbol{\theta}, \cdot)$, such that given a Patterson map \mathbf{p} as input, it generates an estimate of an electron density map, that resembles closely the true map \mathbf{e} . Formally, given a data distribution \mathcal{D} and $\{\mathbf{p}_i, \mathbf{e}_i\}_{i=1}^n \sim \mathcal{D}$, where $\mathbf{p}_i \in \mathbb{R}^{N_1 \times N_2 \times N_3}$ is the Patterson map that corresponds to the true data electron density map, $\mathbf{e}_i \in \mathbb{R}^{N_1 \times N_2 \times N_3}$, deep learning training aims in finding $\boldsymbol{\theta}^*$ as in:

$$\theta^* = \arg \min_{\theta} \left\{ \mathcal{L}(\theta) := \frac{1}{n} \sum_{i=1}^n \ell(\theta; g, \{\mathbf{p}_i, \mathbf{e}_i\}) = \frac{1}{n} \sum_{i=1}^n \|g(\theta, \mathbf{p}_i) - \mathbf{e}_i\|_2^2 \right\}.$$

Since we have a regression problem, we use mean squared error as the loss function $\mathcal{L}(\theta)$.

Using partial protein structures. Due to the well-studied structure of amino acids, we aim to optionally utilize standardized *partial structures* to aid prediction, when they are available. For example, let $\mathbf{u}_i^j \in \mathbb{R}^{N_1 \times N_2 \times N_3}$ be the known standalone electron density map of the j -th amino acid of the i -th protein sample, in a standardized conformation. Abstractly, we then aim to optimize:

$$\theta^* = \arg \min_{\theta} \left\{ \mathcal{L}(\theta) := \frac{1}{n} \sum_{i=1}^n \ell(\theta; g, \{\mathbf{p}_i, \mathbf{e}_i, \mathbf{u}_i^j\}) = \frac{1}{n} \sum_{i=1}^n \|g(\theta, \mathbf{p}_i, \mathbf{u}_i^j) - \mathbf{e}_i\|_2^2 \right\}.$$

Challenges and Design Principles. We face the difficult learning problem to infer electron density maps \mathbf{e} from Patterson maps \mathbf{p} , which involves Fourier transformations. *These transformations can be intuitively considered as transforming local information to global information*, which is rare in common deep model use cases. Secondly, it is nontrivial to incorporate the partial structure density maps \mathbf{u}_i^j to aid prediction. Thirdly, the 3d data format of both our inputs and outputs often increases substantially the computational requirements. Finally, since part of our contributions is novel datasets on this problem, we need to be data efficient due to the expensive dataset creation cost. Thus, the main design principles for our model can be summarized as:

- *Design Principle #1:* Be able to process the global information in Patterson maps to correctly infer the corresponding electron density maps;
- *Design Principle #2:* Be able to incorporate partial structure information, when available;
- *Design Principle #3:* Learn to fulfill the above, with reduced computational and data-creation costs.

Gap in current knowledge. As an initial attempt, the well-established convolution-based U-Net model (Ronneberger et al., 2015) could be utilized for this task. This is the path followed in (Pan et al., 2023). However, classical U-Nets cannot fulfill the design principles above, since: *i*) they mostly rely on local information within CNN layers; such a setup is not suitable when Patterson maps are available, since the latter do not have meaningful local structures. *ii*) It is not clear (or, at best, non-trivial) to incorporate any partial protein structures prior information, since the latter is in a different representation domain, compared to Patterson maps. Finally, *iii*) a large 3d U-Net model is computationally expensive and inefficient, due to the 3d filter convolution computation.

Our proposal: CrysFormer. We propose CrysFormer, a novel, 3d Transformer model (Vaswani et al., 2017; Chen et al., 2021) with a new self-attention mechanism to process Patterson maps and partial protein structures, to directly infer electron density maps with reduced costs.

Inspired by recent research on the potential connection between Fourier transforms and the self-attention mechanism, found in the Transformer model (Lee-Thorp et al., 2022), CrysFormer captures the global information in Patterson maps and “translates” it into correct electron density map predictions, via our proposed self-attention mechanism (*Design Principle #1*). CrysFormer does not need an encoder-decoder structure (Vaswani et al., 2017) and artificial information bottlenecks (Cheng et al., 2019) –as in the U-Net architecture– to force the learning of global information.

By definition, CrysFormer is able to handle additional partial structure information, which comes from a different domain than the Patterson maps (*Design Principle #2*; more details below).

Finally, by using efficient self-attention between 3d image patches, we can significantly reduce the overall computation cost. Detaching our model from an encoder-decoder architecture further reduces the required depth of the model and, thus, the overall training cost (*Design Principle #3*).

The architecture of the CrysFormer. We follow ideas of a 3d visual Transformer (Chen et al., 2021) by partitioning the whole input 3d Patterson map $\mathbf{p}_i \in \mathbb{R}^{N_1 \times N_2 \times N_3}$ input into a set of smaller 3d patches. We embed them into one-dimensional “word tokens”, and feed them into a multi-layer, encoder-only Transformer module. If partial structures \mathbf{u}_i^j are also available, we will partition them into 3d patches and embed them into additional tokens that are sent to each self-attention layer. This way, the tokens in each layer can also “attend” the electron density of partial structures, as a reference

for final global electron density map predictions. Finally, we utilize a 3d convolutional layer to transform “word-tokens” back into a 3d electron density map.² See Figure 1.

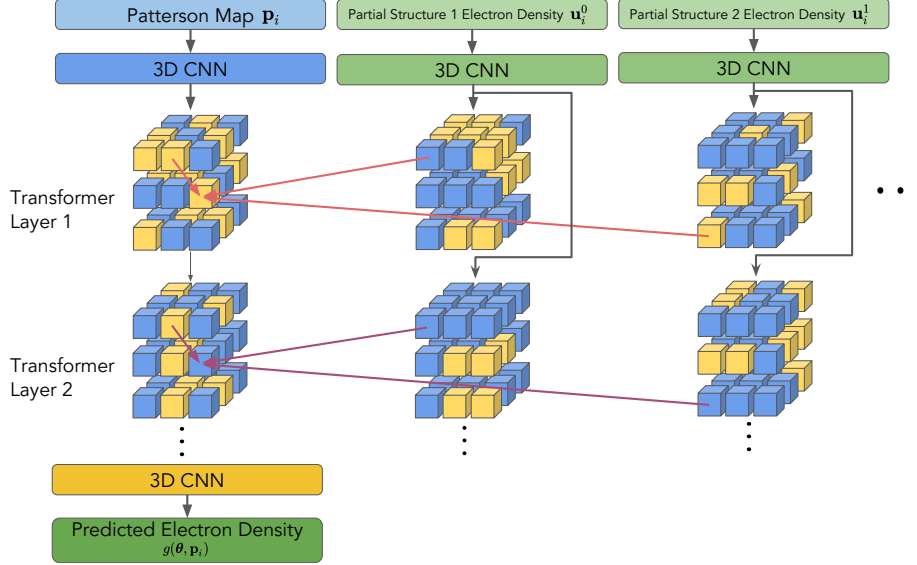


Figure 1: Abstract depiction of the `Crysformer`, which utilizes a one-way attention mechanism (red and purple arrows) to incorporate the partial structure information. The tokens from the additional partial structure all come from initial 3d CNN embedding and are not passed to the next layer.

Mathematically, we report the following: The first part is the preprocessing and partitioning of input Patterson maps \mathbf{p} and additional partial structures \mathbf{u}^j into 3d patches of size $d_1 \times d_2 \times d_3$. We embed those patches into one-dimensional tokens with dimension d_t , using of a small MLP, and add them with a learned positional embedding; this holds for both Patterson maps and structures, as below:

Patterson maps \mathbf{p}	Partial structures \mathbf{u}^j
$\mathbf{X}^0 = 3\text{DCNN}_{\mathbf{w}_c}(\mathbf{p}) \in \mathbb{R}^{c \times N_1 \times N_2 \times N_3}$	$\mathbf{U}^j = 3\text{DCNN}_{\mathbf{w}_p}(\mathbf{u}^j) \in \mathbb{R}^{c \times N_1 \times N_2 \times N_3}$
$\mathbf{X}^0 = \text{Partition}(\mathbf{X}^0) \in \mathbb{R}^{\frac{N_1}{d_1} \times \frac{N_2}{d_2} \times \frac{N_3}{d_3} \times (cd_1 d_2 d_3)}$	$\mathbf{U}^j = \text{Partition}(\mathbf{U}^j) \in \mathbb{R}^{\frac{N_1}{d_1} \times \frac{N_2}{d_2} \times \frac{N_3}{d_3} \times (cd_1 d_2 d_3)}$
$\mathbf{X}^0 = \text{Flatten}(\mathbf{X}^0) \in \mathbb{R}^{\frac{N_1 N_2 N_3}{d_1 d_2 d_3} \times (cd_1 d_2 d_3)}$	$\mathbf{U}^j = \text{Flatten}(\mathbf{U}^j) \in \mathbb{R}^{\frac{N_1 N_2 N_3}{d_1 d_2 d_3} \times (cd_1 d_2 d_3)}$
$\mathbf{X}^0 = \text{MLP}_{\mathbf{w}_c}(\mathbf{X}^0) \in \mathbb{R}^{\frac{N_1 N_2 N_3}{d_1 d_2 d_3} \times d_t}$	$\mathbf{U}^j = \text{MLP}_{\mathbf{w}_p}(\mathbf{U}^j) \in \mathbb{R}^{\frac{N_1 N_2 N_3}{d_1 d_2 d_3} \times d_t}$
$\mathbf{X}^0 = \mathbf{X}^0 + \text{PosEmbedding}(\frac{N_1 N_2 N_3}{d_1 d_2 d_3})$	$\mathbf{U}^j = \mathbf{U}^j + \text{PosEmbedding}(\frac{N_1 N_2 N_3}{d_1 d_2 d_3})$

As shown in Figure 1, we design an efficient attention mechanism such that *i*) only tokens from Patterson maps attend tokens from the partial structures; *ii*) the tokens from the additional partial structures are not passed to the next layer. This is based on that the partial structure electron density information should be used by the model as a stable reference to attend to in each layer.

This one-way attention also greatly reduces the overall communication cost. In particular, let the token sequence length be $S = \frac{N_1 N_2 N_3}{d_1 d_2 d_3}$ and let d_h denote the dimension of the attention head. Assuming we have H attention heads and L layers, `CrysFormer` uses the following attention mechanism:

²We also utilize 3d convolutional layer(s) at the very beginning of the execution to expand the number of channels of the Patterson map (and potentially partial structure) inputs.

$$\begin{aligned}
\mathbf{U} &= \text{Concat}_{j=1}^J(\mathbf{U}^j) \in \mathbb{R}^{(SJ) \times d_t} \\
\mathbf{A}^h &= \text{Softmax}((\mathbf{W}_q^h \mathbf{X}^\ell)^\top (\text{Concat}(\mathbf{W}_k^h \mathbf{X}^\ell, \mathbf{W}_{k'}^h \mathbf{U}))) \in \mathbb{R}^{S \times (S+SJ)}; \\
\widehat{\mathbf{V}}^h &= \mathbf{A}^h (\text{Concat}(\mathbf{W}_v^h \mathbf{X}^\ell, \mathbf{W}_{v'}^h \mathbf{U})) \in \mathbb{R}^{S \times d_h}; \\
\mathbf{O} &= \mathbf{W}_o \text{Concat}(\widehat{\mathbf{V}}^0, \widehat{\mathbf{V}}^1, \dots, \widehat{\mathbf{V}}^H) \in \mathbb{R}^{S \times d_t}; \\
\mathbf{X}^{\ell+1} &= \mathbf{W}_{ff2}(\text{ReLU}(\mathbf{W}_{ff1} \mathbf{O})),
\end{aligned}$$

where, omitting the layer index, \mathbf{W}_q^h , \mathbf{W}_k^h , \mathbf{W}_v^h are the trainable query, key, and value projection matrices of the h -th attention head for tokens from the Patterson map, and $\mathbf{W}_{k'}$, $\mathbf{W}_{v'}$ are the corresponding matrices for tokens from the partial structure, each with dimension d_h . Further, \mathbf{W}_{ff1} and \mathbf{W}_{ff2} are the trainable parameters of the fully-connected layers. We omit skip connections and layer normalization modules just to simplify notation, but these are included in practice.

As a final step, we transform the output embedding back to a 3d electron density map, as follows:

$$g(\boldsymbol{\theta}, \mathbf{p}) = \tanh(3\text{DCNN}_{\mathbf{w}_o}(\text{Rearrange}(\text{MLP}(\mathbf{X}^L)))) \in \mathbb{R}^{N_1 \times N_2 \times N_3},$$

and, as stated previously, we use as our loss function the standard mean squared error loss.

4 NEW DATASETS

We generate datasets of protein fragments, where input Patterson and output electron density maps are derived from Protein Databank (PDB) entries of proteins solved by X-ray Crystallography (wwPDB consortium, 2019). We start from a curated basis of $\sim 24,000$ such protein structures. Then from a random subset of about half of these structures, we randomly select and store segments of adjacent amino acid residues. These examples are consisted of dipeptides (two residues) and 15-residues, leading to two datasets that we introduce with this work. The latter dataset contains 15 residues, where at most 3 residues could be shared between different examples. Using the `pdffixer` Python API (Eastman et al., 2017), we remove all examples that either contain nonstandard residues or have missing atoms from our initial set. We also apply a few standardized modifications.

For our dipeptide dataset, we then iteratively expand the unit cell dimensions for each example, starting from the raw max – min ranges in each of the three axis directions, attempting to create a minimal-size unit cell where the minimum atomic contact is at least 2.75 Angstroms (\AA).³ For our 15-residue dataset, we instead place atoms in fixed unit cells of size $41 \text{\AA} \times 30 \text{\AA} \times 24 \text{\AA}$ to simplify the now much harder problem. After this, all examples that still contain atomic contacts of less than 2.75\AA are discarded. The examples are then reoriented via a reindexing operation, such that the first axis is always the longest and the third axis is always the shortest.

One issue leading to potential ambiguity in interpreting Patterson maps is their invariance to translation of the entire corresponding electron density (Hurwitz, 2020). To tackle this, we center all atomic coordinates such that the center of mass is in the center of the corresponding unit cell. This means that our model’s predicted electron densities would always be more or less centered in the unit cell. We note that this is also the case for the majority of actual protein crystals.

Structure factors for each remaining example, as well as those for the corresponding partial structures for each of the present amino acids, are generated using the `gemmi sfcalc` program (Wojdyr, 2022) to a resolution of 1.5\AA . An electron density and Patterson map for each example are then obtained from those structure factors with the `fft` program of the CCP4 program suite (Read & Schierbeek, 1988; Winn et al., 2011); partial structure densities are obtained in the same manner. We specify a grid oversampling factor of 3.0, resulting in a 0.5\AA grid spacing in the produced maps. All these maps are then converted into PyTorch tensors. We then normalize the values in each of the tensors to be in the range $[-1, 1]$. Since, in our PyTorch implementation, all examples within a training batch are of the same size, we remove all examples from the tensor-size bins containing fewer examples than a specified minimum batch size.

³An Angstrom is a metric unit of length equal to 10^{-10} m.

5 EXPERIMENTS

Baselines. There are no readily available off-the-self solutions for our setting, as our work is one of the first of this kind. As our baseline, we use a CNN-based U-Net model (Pan et al., 2023); this architecture is widely used in image transformation tasks (Ronneberger et al., 2015; Yan et al., 2021).

For comparison, we have further enhanced this vanilla U-Net with *i*) additional input channels to incorporate the partial structure information, despite being evidently unsound; and *ii*) a refining model procedure, which retrains the U-Net using previous model predictions as additional input channels. Both of these extensions are shown to greatly improve the performance of the vanilla U-Net. We refer the reader to the appendix for more details on our baseline model architecture.

Metrics. During testing, we calculate the Pearson correlation coefficient between the ground truth targets \mathbf{e} and model predictions $g(\boldsymbol{\theta}, \mathbf{p})$; the larger this coefficient is, the better. Let us denote a model prediction as \mathbf{e}' . We define $\bar{\mathbf{e}} = \frac{1}{N_1 N_2 N_3} \sum_{i,j,k} \mathbf{e}_{i,j,k}$ and $\bar{\mathbf{e}}' = \frac{1}{N_1 N_2 N_3} \sum_{i,j,k} \mathbf{e}'_{i,j,k}$. Then, the Pearson correlation coefficient between \mathbf{e} and \mathbf{e}' is as below:

$$\text{PC}(\mathbf{e}, \mathbf{e}') = \frac{\sum_{i,j,k=1}^{N_1, N_2, N_3} (\mathbf{e}'_{i,j,k} - \bar{\mathbf{e}}')(\mathbf{e}_{i,j,k} - \bar{\mathbf{e}})}{\sqrt{\sum_{i,j,k=1}^{N_1, N_2, N_3} (\mathbf{e}'_{i,j,k} - \bar{\mathbf{e}}')^2 + \epsilon} \cdot \sqrt{\sum_{i,j,k=1}^{N_1, N_2, N_3} (\mathbf{e}_{i,j,k} - \bar{\mathbf{e}})^2 + \epsilon}}, \quad (4)$$

where ϵ is a small constant to prevent division by zero. To demonstrate how well our methods solve the phase problem, we also perform phase error analysis on our models' final post-training predictions using the `cphasesmatch` program of the CCP4 program suite (Cowtan, 2011). We report the mean phase errors of our predictions in degrees, as reported by `cphasesmatch`, where a smaller phase error is desirable. Finally, we compare the convergence speed and computation cost of both methods.

Method	Mean PC(\mathbf{e}, \mathbf{e}')	Mean Phase Error	Epochs	Time per epoch (mins.)
U-Net (Pan et al., 2023)	0.735	67.40°	50	28.93
U-Net+R (This work)	0.775	58.67°	90	29.06
U-Net+PS+R (This work)	0.839	51.34°	90	29.31
CrysFormer (This work)	0.939	35.16°	35	12.37

Table 1: CrysFormer versus baselines on the dipeptide dataset. U-Net+R refers to adding the refining procedure to U-Net training; U-Net+PS+R refers to adding further partial structures as additional channels.

Results on two-residues. A summary of our results on our dipeptide dataset, which consisted of 1,894,984 training and 210,487 test cases, is provided in Table 1. Overall, CrysFormer achieves a significant improvement in prediction accuracy in terms of both the Pearson coefficient and phase error, while requiring a shorter time (in epochs) to converge. CrysFormer also incurs much less computation cost which results in significantly reduced wall clock time per epoch.

We further visualize some of the predictions in Figure 2, comparing side by side those made by the baselines and the CrysFormer. CrysFormer produces more accurate predictions in terms of both global and local structures. This verifies our hypothesis that *i*) the self-attention mechanism can better capture the global information in Patterson maps, and *ii*) the removal of the U-Net's encoder-decoder structure prevents loss of information and improves the reproduction of finer details.

E.g., the top row of Figure 2 represents a class of examples containing a large aromatic residue, Tryptophan. U-Net+R models consistently produce poor predictions in this case, while the CrysFormer better handles such residues. U-Net+PS+R shows that both providing additional input channels and using the refining procedure improves results even for U-Net architectures; yet, CrysFormer still provides better reconstruction. More visualizations can be found in the appendix.

We further plot the calculated average mean phase errors of the predictions of our models against reflection resolution, see left panel of Figure 3. The predictions made by CrysFormer have lower mean phase error, compared to baselines. This means that the CrysFormer predictions, on average, can reproduce better the general shape, as well as finer details of the ground truth electron densities.

Finally, we generate a chart of the fraction of our models' predictions for which the calculated mean phase error is $< 60^\circ$ at various ranges of resolution. We consider such predictions to accurately reproduce the level of detail specified by that resolution range. This is shown on the right panel in Figure 3. At all resolution ranges, CrysFormer predictions are clearly better than that of the

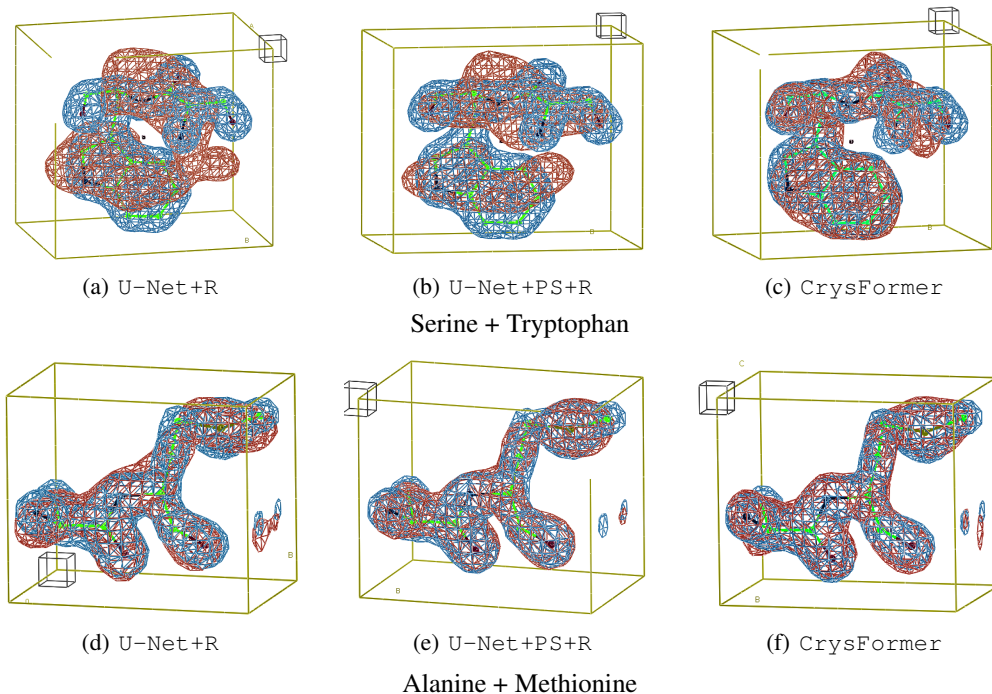


Figure 2: Visualization of electron density predictions for baselines and CrysFormer: Ground truth density maps are shown in blue, while predictions are shown in red. The model used to generate the ground truth electron density is shown in stick representation for reference.

U-Net-based models. In particular, for CrysFormer, we still have a majority of predictions with phase error $< 60^\circ$ even at the highest ranges of resolution.

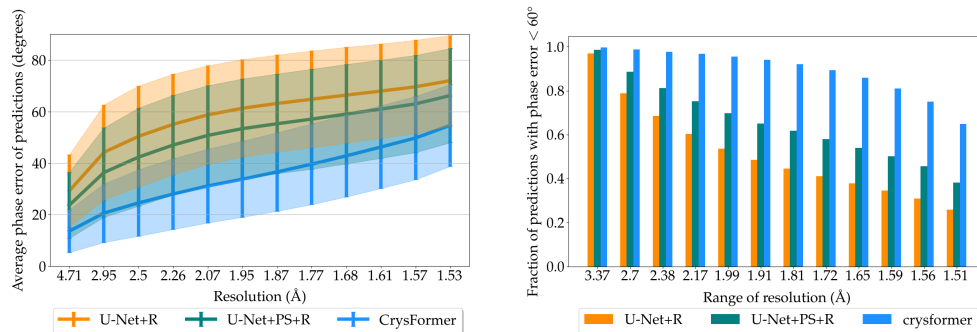


Figure 3: Dipeptide dataset. **Left:** Average phase error of model predictions against reflection resolution. **Right:** Fraction of model predictions for which phase error is $< 60^\circ$ at various ranges of resolution.

Results on 15-residues. On our dataset of 15-residue examples, which consisted of only 165,858 training and 16,230 test cases (less than one-tenth the size of our dipeptide dataset), we trained for 80 epochs to a final average test set Pearson correlation of about 0.747. We then performed a refining training run of 20 epochs, incorporating the original training run’s predictions as additional input channels when training the CrysFormer, and obtained an improved average test set Pearson correlation of about 0.77 and phase error of about 67.66. On both of these runs, we used the Nyström approximate attention mechanism (Xiong et al., 2021) when incorporating our partial structure information to reduce time and space costs. Even still, each training epoch still took about 6.28 hours to complete. Thus due to time considerations, we decided not to attempt to train a U-Net on this dataset for purposes of comparison.

We provide visualizations of some model predictions in Figure 4; more can again be found in the appendix. We also plot the average mean phase errors of the predictions of our models against reflection resolution, as well as the fraction of our models’ predictions for which the calculated mean phase error is $< 60^\circ$ at various ranges of resolution in Figure 5. These results show that this is a

more difficult dataset with reduced sample size; yet `CrysFormer` predictions tend to accurately reproduce details of the desired electron densities.

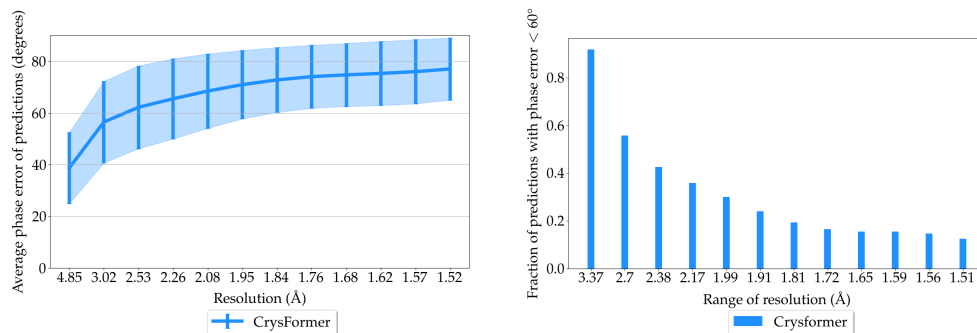


Figure 5: **Left:** Average phase error of model predictions on 15-residue dataset against reflection resolution. **Right:** Fraction of model predictions on 15-residue dataset for which phase error is $< 60^\circ$ at various ranges of resolution.

We used the *Autobuild* program within the *PHENIX* suite (Terwilliger et al., 2008; Liebschner et al., 2019) to perform automated model building and crystallographic refinement on a randomly selected subset of 302 test set predictions after the refining training run. We found that 281 out of 302 ($\sim 93\%$) refined to a final atomic model with a crystallographic R -factor of less than 0.38, indicating success, when solvent flattening was applied. Without solvent flattening, 258 out of 302 ($\sim 85\%$) refined to such an R -factor (performing solvent flattening is known to be especially effective for unit cells with high solvent content, i.e. a large amount of empty space around the atoms). Figure 6 shows these results as scatterplots; clearly only a small fraction of the subset of predictions did not refine successfully. And even if no refinement was performed at all, and instead an atomic model was repeatedly fit to our predicted electron densities, we found that 229 out of 302 ($\sim 76\%$) of the best such atomic models still had a crystallographic R -factor of less than 0.38.

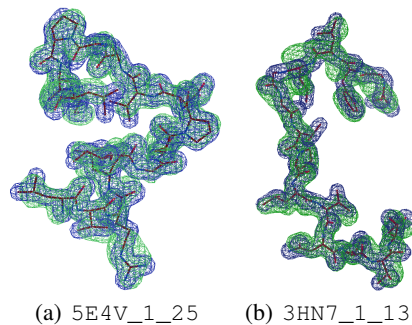


Figure 4: Visualization of two successful predictions after a refining training run; ground truth density maps shown in blue and predictions shown in green.

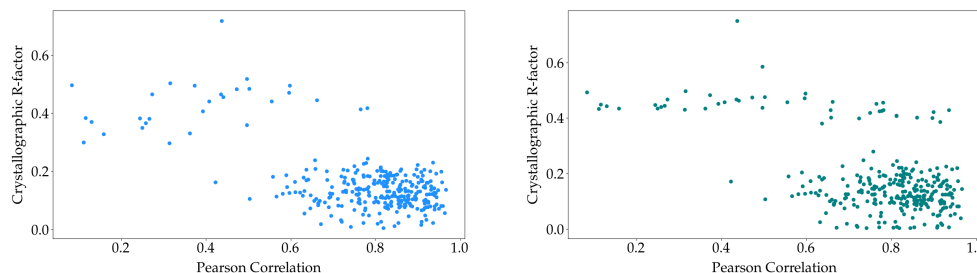


Figure 6: **Left Panel:** Scatterplot of post-refinement model R -factors, with solvent flattening applied. **Right Panel:** Scatterplot of post-refinement model R -factors, without solvent flattening applied

Furthermore, after automatic map interpretation using the autobuilding routines in *shelxe* (Usón & Sheldrick, 2018) to obtain a poly-alanine chain from each of the 16230 test set predictions, we found that almost 74% of the resulting models had calculated amplitudes with a Pearson correlation of at least 0.25 to the true underlying data. Historical results indicate that further refinement would very likely produce a "correct" model if the initial poly-alanine model has at least such a correlation.

6 DISCUSSION

We have shown that `CrysFormer` outperforms state of the art models for predicting electron density maps from corresponding Patterson maps in all metrics on a newly introduced dataset (dipeptide). Overall, `CrysFormer` requires fewer epochs to reasonably converge and has a smaller

computational footprint. Furthermore, our “refining” procedure greatly improves training for the vanilla U-Net architecture on our dipeptide dataset, as well as for training `CrysFormer` on our both dipeptide and 15-residues dataset.

Limitations and next steps. Following successful results on our initial 15-residue dataset, we also suggest training our model on variable unit cells at that problem size as future work. Eventually, we also prefer handling variable cell angles as well, moving beyond the orthorhombic crystal system. We will explore changing the formulation of our partial structures to have more than one amino acid residue in a structure, as having each partial structure representing only a single residue may no longer be reasonable, both computationally and from a practical perspective.

Broader Impacts. Solving the crystallographic phase problem for proteins would dramatically reduce the time and expense of determining a new protein structure, especially if there are no close homologs already in the Protein Data Bank. There exist some methods that sometimes work under special conditions Jiang et al. (2018), or that work sometimes but only at very low resolutions David & Subbiah (1994). The recent line of work on AlphaFold Jumper et al. (2021); Tunyasuvunakool et al. (2021) definitely helps in these problems; we note though that this is true mostly in cases where reliable predictions are possible due to strong homologs and/or extensive sequence data.

REFERENCES

- Neil W Ashcroft and N David Mermin. *Solid state physics*. Cengage Learning, 2022.
- Emiliano Brini, Carlos Simmerling, and Ken Dill. Protein storytelling through physics. *Science*, 370(6520):eaaz3041, 2020.
- Emmanuel J Candes, Thomas Strohmer, and Vladislav Voroninski. Phaselift: Exact and stable signal recovery from magnitude measurements via convex programming. *Communications on Pure and Applied Mathematics*, 66(8):1241–1274, 2013.
- Emmanuel J Candes, Xiaodong Li, and Mahdi Soltanolkotabi. Phase retrieval via wirtinger flow: Theory and algorithms. *IEEE Transactions on Information Theory*, 61(4):1985–2007, 2015.
- Junyu Chen, Yufan He, Eric C. Frey, Ye Li, and Yong Du. Vit-v-net: Vision transformer for unsupervised volumetric medical image registration. *arXiv*, .2104.06468, 2021. URL <https://doi.org/10.48550/arXiv.2104.06468>.
- Hao Cheng, Dongze Lian, Shenghua Gao, and Yanlin Geng. Utilizing information bottleneck to evaluate the capability of deep neural networks for image classification. *Entropy*, 21(5), 2019. ISSN 1099-4300. doi: 10.3390/e21050456. URL <https://www.mdpi.com/1099-4300/21/5/456>.
- Kevin Cowtan. cphasematch, 2011. URL <https://www.ccp4.ac.uk/html/cphasematch.html>.
- P. R. David and S. Subbiah. Low-resolution real-space envelopes: the application of the condensing-protocol approach to the *ab initio* macromolecular phase problem of a variety of examples. *Acta Crystallographica Section D*, 50(2):132–138, Mar 1994. doi: 10.1107/S090744499301131X. URL <https://doi.org/10.1107/S090744499301131X>.
- Jan Drenth. *Principles of protein X-ray crystallography*. Springer Science & Business Media, 2007.
- Peter Eastman, Jason Swails, John D Chodera, Robert T McGibbon, Yutong Zhao, Kyle A Beauchamp, Lee-Ping Wang, Andrew C Simmonett, Matthew P Harrigan, Chaya D Stern, et al. Openmm 7: Rapid development of high performance algorithms for molecular dynamics. *PLoS computational biology*, 13(7):e1005659, 2017.
- J. R. Fienup. Phase retrieval algorithms: a comparison. *Appl. Opt.*, 21(15):2758–2769, Aug 1982. doi: 10.1364/AO.21.002758.
- Youming Guo, Yu Wu, Ying Li, Xuejun Rao, and Changhui Rao. Deep phase retrieval for astronomical Shack–Hartmann wavefront sensors. *Monthly Notices of the Royal Astronomical Society*, 510(3): 4347–4354, 12 2021. ISSN 0035-8711. doi: 10.1093/mnras/stab3690.
- Hongxing He and Wu-Pei Su. Direct phasing of protein crystals with high solvent content. *Acta Crystallographica Section A*, 71(1):92–98, Jan 2015. doi: 10.1107/S2053273314024097.
- Hongxing He, Hengrui Fang, Mitchell D Miller, George N Phillips Jr, and W-P Su. Improving the efficiency of molecular replacement by utilizing a new iterative transform phasing algorithm. *Acta Crystallographica Section A: Foundations and Advances*, 72(5):539–547, 2016.
- Kaiming He, Xiangyu Zhang, Shaoqing Ren, and Jian Sun. Delving deep into rectifiers: Surpassing human-level performance on imagenet classification. In *2015 IEEE International Conference on Computer Vision (ICCV)*, pp. 1026–1034, New York, NY, USA, 2015. IEEE Press. doi: 10.1109/ICCV.2015.123.
- Anne Marie Helmenstine. Amino acid chirality, 2021. URL <https://www.thoughtco.com/amino-acid-chirality-4009939>.
- Jie Hu, Li Shen, and Gang Sun. Squeeze-and-excitation networks. In *2018 IEEE/CVF Conference on Computer Vision and Pattern Recognition*, pp. 7132–7141, New York, NY, USA, 2018. IEEE Press. doi: 10.1109/CVPR.2018.00745.

-
- David Hurwitz. From patterson maps to atomic coordinates: Training a deep neural network to solve the phase problem for a simplified case. *arXiv*, 03 2020.
- Mengchao Jiang, Hongxing He, Yunpeng Cheng, and Wu-Pei Su. Resolution dependence of an ab initio phasing method in protein x-ray crystallography. *Crystals*, 8(4), 2018. ISSN 2073-4352. doi: 10.3390/cryst8040156. URL <https://www.mdpi.com/2073-4352/8/4/156>.
- Shikai Jin, Mitchell D Miller, Mingchen Chen, Nicholas P Schafer, Xingcheng Lin, Xun Chen, GN Phillips, and PG Wolynes. Molecular-replacement phasing using predicted protein structures from awsem-suite. *IUCrJ*, 7(6):1168–1178, 2020.
- John Jumper, Richard Evans, Alexander Pritzel, Tim Green, Michael Figurnov, Olaf Ronneberger, Kathryn Tunyasuvunakool, Russ Bates, Augustin Žídek, Anna Potapenko, Alex Bridgland, Clemens Meyer, Simon A. A. Kohl, Andrew J. Ballard, Andrew Cowie, Bernardino Romera-Paredes, Stanislav Nikolov, Rishub Jain, Jonas Adler, Trevor Back, Stig Petersen, David Reiman, Ellen Clancy, Michal Zielinski, Martin Steinegger, Michalina Pacholska, Tamas Berghammer, Sebastian Bodenstern, David Silver, Oriol Vinyals, Andrew W. Senior, Koray Kavukcuoglu, Pushmeet Kohli, and Demis Hassabis. Highly accurate protein structure prediction with alphafold. *Nature*, 596(7873):583–589, 2021.
- Armin Kappeler, Sushobhan Ghosh, Jason Holloway, Oliver Cossairt, and Aggelos Katsaggelos. Ptychnet: Cnn based fourier ptychography. In *2017 IEEE International Conference on Image Processing (ICIP)*, pp. 1712–1716, New York, NY, USA, 2017. IEEE Press.
- Richard Lawrence Kingston and Rick P Millane. A general method for directly phasing diffraction data from high-solvent-content protein crystals. *IUCrJ*, 9(5), 2022.
- Eaton Lattman and Patrick Loll. *Protein Crystallography*. Johns Hopkins University Press, 2008.
- James Lee-Thorp, Joshua Ainslie, Ilya Eckstein, and Santiago Ontanon. Fnet: Mixing tokens with fourier transforms, 2022.
- Dorothee Liebschner, Pavel V. Afonine, Matthew L. Baker, Gábor Bunkóczi, Vincent B. Chen, Tristan I. Croll, Bradley Hintze, Li-Wei Hung, Swati Jain, Airlie J. McCoy, Nigel W. Moriarty, Robert D. Oeffner, Billy K. Poon, Michael G. Prisant, Randy J. Read, Jane S. Richardson, David C. Richardson, Massimo D. Sammito, Oleg V. Sobolev, Duncan H. Stockwell, Thomas C. Terwilliger, Alexandre G. Urzhumtsev, Lizbeth L. Videau, Christopher J. Williams, and Paul D. Adams. Macromolecular structure determination using x-rays, neutrons and electrons: recent developments in phenix. *Acta Crystallogr.*, D75(10):861–877, Oct 2019. doi: 10.1107/S2059798319011471. URL <https://doi.org/10.1107/S2059798319011471>.
- Tom Pan, Shikai Jin, Mitchell D Miller, Anastasios Kyrillidis, and George N Phillips. A deep learning solution for crystallographic structure determination. *IUCrJ*, 10(4):487–496, 2023.
- A. L. Patterson. A fourier series method for the determination of the components of interatomic distances in crystals. *Phys. Rev.*, 46:372–376, Sep 1934. doi: 10.1103/PhysRev.46.372.
- RJ Read and AJ Schierbeek. A phased translation function. *Journal of Applied Crystallography*, 21(5):490–495, 1988.
- Yair Rivenson, Yibo Zhang, Harun Günaydın, Da Teng, and Aydogan Ozcan. Phase recovery and holographic image reconstruction using deep learning in neural networks. *Light: Science & Applications*, 7(2):17141–17141, 2018.
- Olaf Ronneberger, Philipp Fischer, and Thomas Brox. U-net: Convolutional networks for biomedical image segmentation. In *Medical Image Computing and Computer-Assisted Intervention—MICCAI 2015: 18th International Conference, Munich, Germany, October 5-9, 2015, Proceedings, Part III 18*, pp. 234–241, 2015.
- Amrith Roy, Alper Kucukural, and Yang Zhang. I-TASSER: a unified platform for automated protein structure and function prediction. *Nature protocols*, 5(4):725–738, 2010.
- Andrej Šali and Tom L Blundell. Comparative protein modelling by satisfaction of spatial restraints. *Journal of molecular biology*, 234(3):779–815, 1993.

-
- Manfred J Sippl. Calculation of conformational ensembles from potentials of mean force: an approach to the knowledge-based prediction of local structures in globular proteins. *Journal of molecular biology*, 213(4):859–883, 1990.
- Charles Tanford and Jacqueline Reynolds. *Nature's Robots: A History of Proteins*. Oxford University Press, 2004.
- Thomas C. Terwilliger, Ralf W. Grosse-Kunstleve, Pavel V. Afonine, Nigel W. Moriarty, Peter H. Zwart, Li-Wei Hung, Randy J. Read, and Paul D. Adams. Iterative model building, structure refinement and density modification with the *PHENIX AutoBuild* wizard. *Acta Crystallogr.*, D64(1): 61–69, Jan 2008. doi: 10.1107/S090744490705024X. URL <https://doi.org/10.1107/S090744490705024X>.
- Thomas C. Terwilliger, Dorothee Liebschner, Tristan I. Croll, Christopher J. Williams, Airlie J. McCoy, Billy K. Poon, Pavel V. Afonine, Robert D. Oeffner, Jane S. Richardson, Randy J. Read, and Paul D. Adams. Alphafold predictions are valuable hypotheses, and accelerate but do not replace experimental structure determination. *bioRxiv*, 2023. doi: 10.1101/2022.11.21.517405. URL <https://www.biorxiv.org/content/early/2023/05/19/2022.11.21.517405>.
- Kathryn Tunyasuvunakool, Jonas Adler, Zachary Wu, Tim Green, Michal Zielinski, Augustin Židek, Alex Bridgland, Andrew Cowie, Clemens Meyer, Agata Laydon, et al. Highly accurate protein structure prediction for the human proteome. *Nature*, 596(7873):590–596, 2021.
- Isabel Usón and George M. Sheldrick. An introduction to experimental phasing of macromolecules illustrated by *SHELX*; new autotracing features. *Acta Crystallogr.*, D74(2):106–116, Feb 2018. doi: 10.1107/S2059798317015121. URL <https://doi.org/10.1107/S2059798317015121>.
- Ashish Vaswani, Noam Shazeer, Niki Parmar, Jakob Uszkoreit, Llion Jones, Aidan N Gomez, Łukasz Kaiser, and Illia Polosukhin. Attention is all you need. *Advances in neural information processing systems*, 30, 2017.
- Martyn D. Winn, Charles C. Ballard, Kevin D. Cowtan, Eleanor J. Dodson, Paul Emsley, Phil R. Evans, Ronan M. Keegan, Eugene B. Krissinel, Andrew G. W. Leslie, Airlie McCoy, Stuart J. McNicholas, Garib N. Murshudov, Navraj S. Pannu, Elizabeth A. Potterton, Harold R. Powell, Randy J. Read, Alexei Vagin, and Keith S. Wilson. Overview of the *CCP4* suite and current developments. *Acta Crystallographica Section D*, 67(4):235–242, Apr 2011. doi: 10.1107/S0907444910045749.
- Marcin Wojdyr. Gemmi: A library for structural biology. *Journal of Open Source Software*, 7(73): 4200, 2022.
- wwPDB consortium. Protein Data Bank: the single global archive for 3D macromolecular structure data. *Nucleic Acids Research*, 47(D1):D520–D528, 2019. doi: 10.1093/nar/gky949. URL <https://doi.org/10.1093/nar/gky949>.
- Yunyang Xiong, Zhanpeng Zeng, Rudransis Chakraborty, Mingxing Tan, Glenn Fung, Yin Li, and Vikas Singh. Nyströmformer: A nyström-based algorithm for approximating self-attention. *Proceedings of the AAAI Conference on Artificial Intelligence*, 35(16):14138–14148, May 2021. doi: 10.1609/aaai.v35i16.17664. URL <https://ojs.aaai.org/index.php/AAAI/article/view/17664>.
- Weidan Yan, Can Chen, and Dengyin Zhang. U-net-based medical image segmentation algorithm. In *13th International Conference on Wireless Communications and Signal Processing (WCSP)*, pp. 1–5, 2021. doi: 10.1109/WCSP52459.2021.9613447.
- Zeev Zalevsky, David Mendlovic, and Rainer G Dorsch. Gerchberg–saxton algorithm applied in the fractional fourier or the fresnel domain. *Optics Letters*, 21(12):842–844, 1996.

A APPENDIX

B MODEL ARCHITECTURE OF BASELINE U-NET MODEL

Our U-net architecture can be divided into three phases. The *Encoding Phase* consists of two $7 \times 7 \times 7$ convolutional layers. The first has 25 output channels while the second has 30 output channels, and both are followed by the standard batch normalization and a ReLU activation. Then, a max pooling operation with kernel size $2 \times 2 \times 2$ and stride 2 is used to reduce the height, width, and depth dimensions by a factor of 2.

The *Learning Features Phase* consists of a sequence of 7 residual blocks. Each of these blocks consists of a $7 \times 7 \times 7$ convolutional layer with 30 output channels followed by batch normalization and ReLU activation, and then another 30-channel $7 \times 7 \times 7$ convolutional layer with batch normalization but no activation. A squeeze and excitation block Hu et al. (2018) occurs at this point, applied with the channel dimension reduced by a factor of 2. Afterward, the residual skip connection is applied, followed by another ReLU activation. At the end of this phase, a naive upsampling operation is used to increase the height, width, and depth dimensions by a factor of 2, thus restoring the original dimensions.

The *Decoding Phase* consists of two $5 \times 5 \times 5$ convolutional layers. The first has 25 output channels and is followed by batch normalization and a ReLU activation, while the second produces the model predictions and thus has only a single output channel. Since all elements of the target outputs were constrained to be in the range $[-1, 1]$, we apply a final tanh activation function after this layer.

In all convolutional layers, the input is "same" padded to preserve height, width, and depth dimensionality. Also, the convolutional layers in the encoding and learning features phases are padded using torch's circular padding scheme to account for the periodic nature of the input Patterson maps. Furthermore, all convolutional layers were initialized using the kaiming_normal function of the default torch.nn module He et al. (2015). As with the CrysFormer, our U-net model is robust to training batches of examples with differing height, width, and depth shapes.

C ADDITIONAL DETAILS ON DATASET GENERATION

To start preparing our dataset, we selected nearly 24000 representative Protein Data Bank (PDB) entries using the following criteria: proteins solved by X-ray crystallography after 1995, sequence length ≥ 40 , refinement resolution ≤ 2.75 , refinement R-Free ≤ 0.28 , with clustering at 30% sequence identity. The standardized modifications we applied to each viable coordinate file were as follows: all temperature factors were set to 20, any selenomethionine residues were rebuilt as methionine, and all hydrogen atoms were removed leaving only carbon, nitrogen, oxygen, and potentially sulfur.

In our dataset generation process, an effort was taken to ensure diversity by sampling from PDB entities with low sequence similarity to each other. However, both test and training sets are taking random samples from the conformations allowed in rotamer and Ramachandran space. Any similar conformations would be expected to be in a different rotational orientation in the cell by the nature of the selection process. We did not compute all-versus-all clustering or force the test and training sets to sample distinct conformational regions. For our 15-residue dataset, in order to obtain a greater amount of starting coordinate files, we allowed at most 3 residues to be shared between distinct examples. To prevent potential overfitting that could arise from this sharing of subsegments, we enforced that all examples derived from the same initial .pdb file would be placed together in either the training or test set.

Another issue regarding ambiguity in Patterson map interpretation is the fact that an electron density will always have the exact same Patterson map as its corresponding centrosymmetry-related electron density. Hurwitz (2020) provided a workaround that involved combining a set of atoms with the set of its centrosymmetry-related atoms into a single example output. However, this also requires a separate post-processing algorithm to separate the original and centrosymmetric densities for each of his model's predictions. Since we are working with real-world structures—rather than randomly placed data—we can exploit their known properties. In particular, we know that all proteinogenic amino acids are naturally found in only one possible enantiomeric configuration (Helmenstine, 2021).

Although the mirror-image symmetry of enantiomers is not exactly the same as centrosymmetry, we show that this is enough to allow us to work with true electron densities of protein fragments.

D DESCRIPTION OF DATASET SUBSET

Due to limitations of online storage space, we provide a subset of our generated dataset. This subset represents a total of 200000 dipeptide examples. As expected, `patterson.tar.gz` contains the generated Patterson maps, while `electron_density.tar.gz` contains the corresponding electron densities. Meanwhile, `partial_structure.tar.gz` contains both of the partial structures for each dipeptide example in the subset.

The dataset can be downloaded through this link:

https://drive.google.com/drive/folders/1X7YkxDd7yTC1RTG1z3NbdRIfKLfFtkrx?usp=share_link

We will also provide a dataset of prepared `.pdb` coordinate files of 15-residue examples, to which our dataset generation process can be applied in order to produce Patterson map and electron density tensors.

E ADDITIONAL VISUALIZATIONS OF MODEL PREDICTIONS

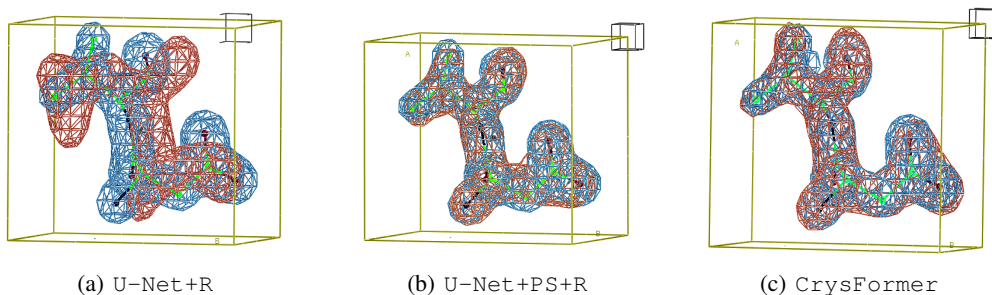


Figure 7: Aspartic Acid + Valine

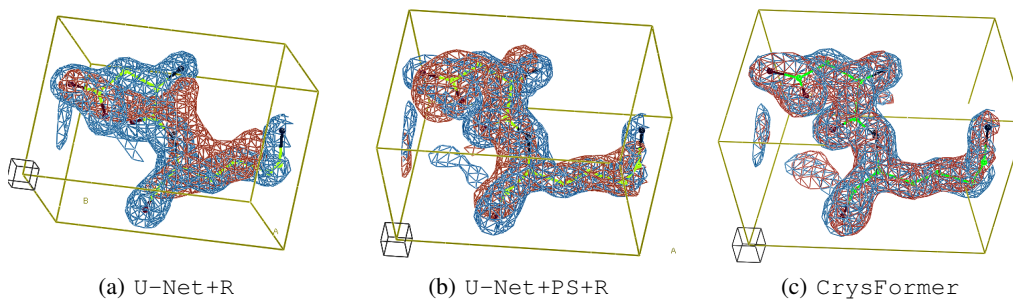


Figure 8: Aspartic Acid + Lysine

Figure 9: Visualizations for dipeptide dataset. Ground truth density maps are shown in blue, while predictions are shown in red. The model used to generate the ground truth electron density is shown in stick representation for reference.

Figure 7 represents an example in which the additional partial structure input channels provided to the U-Net provided a substantial increase in prediction quality, allowing it to produce a prediction similar to that of the `CrysFormer`. Figure 8 represents an example in which both providing additional input channels to the U-Net and switching to `CrysFormer` provided noticeable improvements in prediction quality.

It is clear that as prediction quality increases as indicated by reported Pearson correlation, finer details of the true underlying structure are more likely to be accurately reproduced. The predictions in Figure 10 (e), (f), (g), and (h), as well as Figure 4 (a) [rank 55%] and (b) [rank 82%], were all successfully refined using all of the mentioned autotracing and refinement procedures. But even for relatively

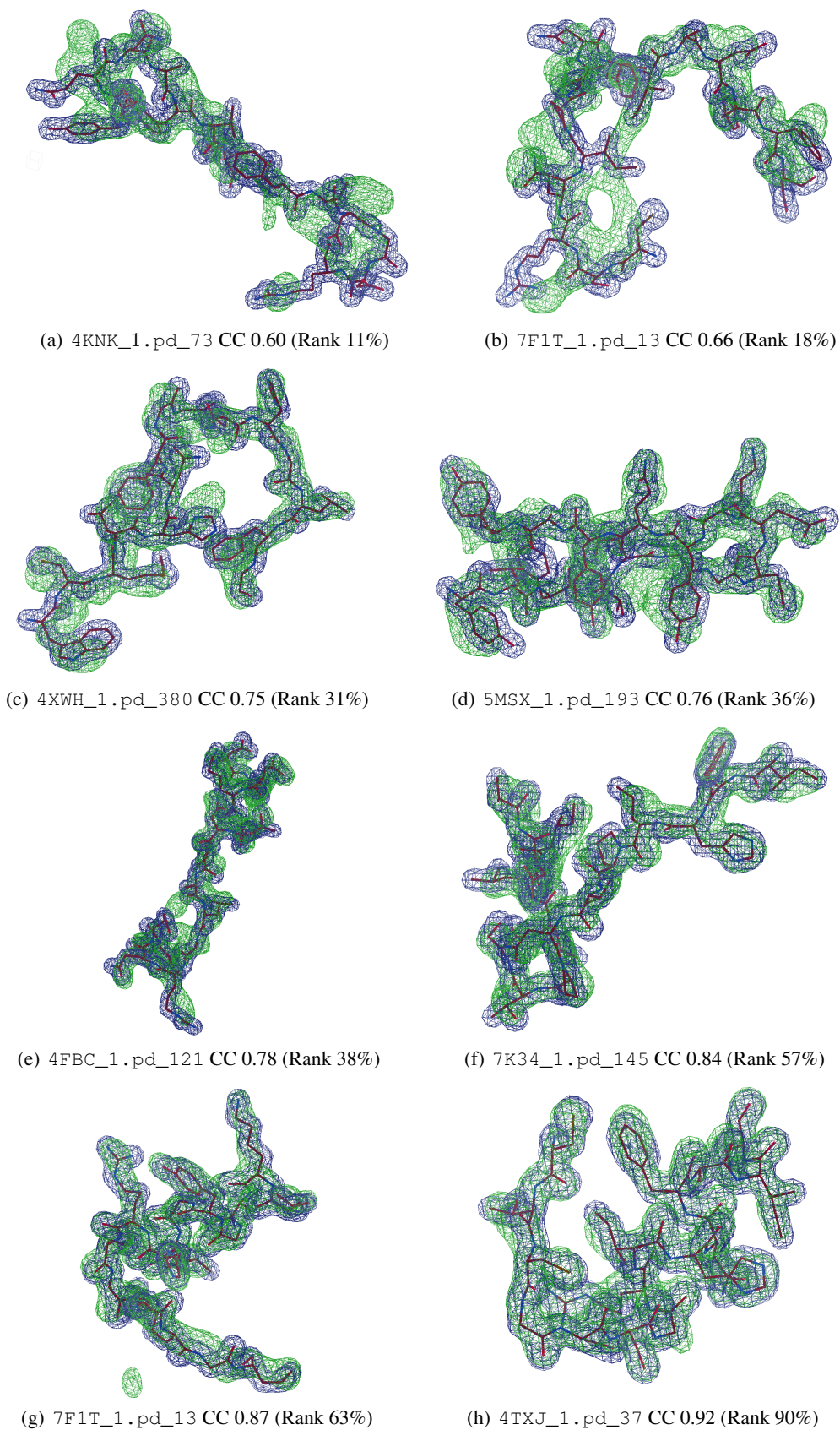


Figure 10: Visualizations for 15-residue dataset. Ground truth density maps are shown in blue, while predictions are shown in green. The model used to generate the ground truth electron density is shown in stick representation.

poor predictions such as (a) and (b), the rough overall shape can be reproduced even though several portions have clear inaccuracies.

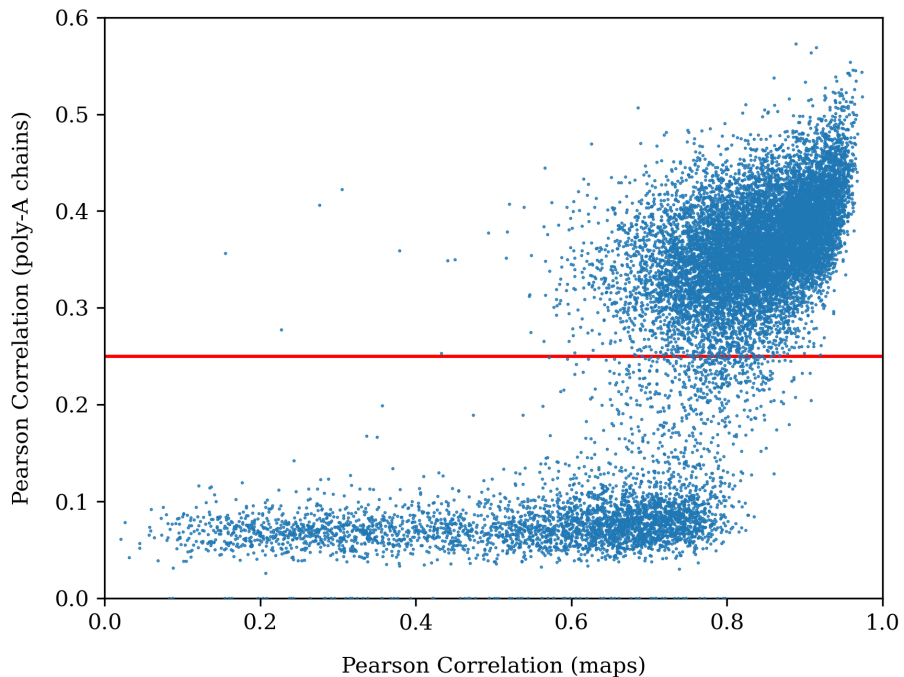


Figure 11: Scatterplot of the Pearson correlations of amplitudes of the poly-alanine chains autotraced by *shelxe* to the ground truth amplitudes vs the Pearson correlation of the predicted and ground truth maps for all 16,203 test cases

Figure 11 shows the scatterplot of *shelxe* poly-alanine autotracing results on the full 15-residue test set. As mentioned, examples for which the amplitudes calculated from the initial poly-alanine chain built into the model electron density prediction have a Pearson correlation coefficient with the true underlying structure factor amplitudes of over 0.25 (shown above the red line) are extremely likely to be successfully refined.